Insight into the inner structure of stretched premixed ammonia-air flames

Alka Karan, Guillaume Dayma, Christian Chauveau, Fabien Halter

Insight into the inner structure of stretched premixed ammonia-air flames

Alka Karan[a*], Guillaume Dayma[a], Christian Chauveau[b], Fabien Halter[a]

[a]*Université d'Orléans, CNRS-ICARE, 1c avenue de la Recherche Scientifique, F-45071 Orléans cedex, France*

[b]*CNRS-ICARE, 1c avenue de la Recherche Scientifique, F-45071 Orléans cedex, France*

Abstract

Ammonia as a fuel has sparked significant interest in the combustion community. Although, using ammonia has a lot of advantages including no carbon emissions, ammonia-air flames are characterized as thick flames with low flame speeds. It is important to understand the flame structure to know the combustion process better. Flame thickness is an important property of the flame which characterizes the reactivity of the flame. Identifying the preheat zone is necessary to determine the fresh gas surface which is used to determine flame speed. Also, understanding the behavior of the important species emitted helps to demonstrate the reaction pathway which may be implemented in chemical kinetics schemes. Further, it is interesting to know the effect of curvature on the emission of excited species which gives direct knowledge on the influence of curvature on the flame reactivity. It was seen that the change in reactivity was manifested as a change in thickness of the species. The experiments presented here were performed on a Bunsen burner at atmospheric conditions. The laminar flame speeds have been evaluated over a range of equivalence ratios by choosing the isotherm as specified by the definition of the flame speed which are slightly higher than the values obtained from the literature. Chemiluminescence from NH* and NH_2* was studied for different equivalence ratios. A 1D simulation performed in Chemkin-*Pro* was used to compare the behavior of the counterpart non-excited species. This comparison helps to correlate excited and non-excited species and also to define the structure of the ammonia-air flame. Both NH* and NH_2* have been determined as heat release rate markers.

Keywords: Ammonia; Flame thickness; Flame speed; Chemiluminescence; Flame structure; Curvature effect

*Corresponding author.

1. Introduction

In the quest of searching for alternative fuels, ammonia combustion has been receiving widespread attention as it is a carbon-free fuel. It is important to study the flame structure and other characteristics to understand the combustion process better and to enhance the performance in energy-based applications. Determining the flame speed is important as it is one of the basic parameters which is used for assessing the characteristics of fuel and engine sizing. It is known that ammonia-air flames have very low flame speed values as reported in the literature. It is also understood that these flames are thicker than hydrocarbon flames [1]. Flame speed is generally evaluated for an isotherm that is as close as possible to the fresh gas's temperature. The error associated with finding the values of the flame speed by not choosing the right isotherm can be large which can lead to huge errors in the assessment of other parameters based on the flame speed. The laminar flame speed, S_L, is defined as the propagation speed relative to the unburnt mixture of a steady, laminar, 1D, planar, stretch-free, and adiabatic flame. Hence, the required isotherm is the one at the fresh gas surface for which defining the flame thickness is needed.

From the emission spectra of ammonia-air flames, NH* and NH_2* have been recognized as species of interest to study. Extensive work on the chemiluminescence of species in ammonia/air and other blended fuels [2-3] can be found in the literature. Pugh et al. [4] used chemiluminescence in both NH_3/air and NH_3/H_2/air to quantify NO in a combustor. Zhu et al. [5] obtained OH* to quantify NO in NH_3/H_2/air flames. NH_2* chemiluminescence has also been used to study NO emissions in plasma-assisted ammonia combustion [6]. Wiseman et al. [7] showed that OH* can be used to compare the flame topology before the blowout. Chemiluminescence from various species [8] was used to study radical formation in high-temperature reactions for NH_3/CH_4 blends in swirl flows both experimentally and numerically and also to determine the location of the highest heat release rate. The chemiluminescence of selected species may be essential to characterize the flame stability and heat release. To our knowledge, no information on HRR and the curvature effect on species via chemiluminescence is available for ammonia/air flames.

DNS studies [9] were performed to study the curvature effects on NO formation in $NH_3/H_2/N_2$/air flames. Studies on extinction stretch rate in both premixed and non-premixed NH_3/CH_4 flames were done experimentally using OH and NO PLIF and numerically using four of the mechanisms existing in literature by Colson et al. [10]. Rocha et al. [11] gave a joint experimental and DNS study on premixed NH_3/CH_4 flames to characterize the structure of the blended flame accommodating the local flame stretch. NH and NO profiles were measured using PLIF. The molecular beam mass spectroscopy was used by Duynslaegher et al. [12] to study the structure of $NH_3/H_2/Ar/O_2$ flames along with the stretch effects. Numerical simulations were also performed to compare with their experimental study. Premixed NH_3/air flame structure was investigated [13] using LIF to obtain profiles of OH, NH, and NO which were used to evaluate four kinetic models. Wolfhard and Parker [14] carried out a spectroscopic investigation into the structure of flat diffusion ammonia-oxygen flame. The work presented here comprises the use of chemiluminescence to study the curvature effect of different excited species and to understand the structure of ammonia-air flames at atmospheric conditions on a Bunsen burner.

2. Methodology

2.1 Experimental set-up

The most common methods to determine the laminar flame speed experimentally include closed spherical constant pressure chamber, stagnation/ counterflow method, heat flux burner, Bunsen burner, and externally heated channel. The apparatus used here consists of a Bunsen burner along with a co-flow of a stoichiometric methane-air pilot flame. The pilot flame emits a power of 55 W which is required to stabilize the NH_3/air flame. The power emitted by the main flame is in between 83 and 117 W. Several studies [4,15] show the use of pilot flame to stabilize the main flame. Although, the power emitted by the pilot flame in the present configuration is about half of what is emitted by the main flame, it can be safe to say that this power has no direct influence on the characteristics of the main flame. It was seen that on changing the power of the pilot flame did not result in change of any of behavior of the parameters used in this study. Moreover, these studies were carried out away from the base of the main flame. The heat losses to the burner is not considered for the same reason. The radiation effects may occur in the burnt gases from the water vapor. For this study, these effects are not of concern as the region of interest is restricted to the initial part of the reaction zone which is away from the burnt gases. The mean velocity of the fresh gases at the exit of the burner ranged from 0.18 to 0.2 m s^{-1}. The fresh gas mixture is injected through the sides of the burner which further flows through a 5 mm thick aluminum grid to obtain a laminar flow. This reactive flow is ignited at the exit of the burner by the presence of the pilot flame. The diameter of the burner outlet is 15 mm. It was observed that the flame flickered by large amounts. This flickering of the flame is attributed to the buoyancy-driven effect. A 150 mm high cylinder with an outer diameter of 120 mm and thickness of 1 mm was mounted at a height of 25 mm from the burner exit which acted as a chimney and helped to reduce the entrainment of air. The flame speed was determined using a PIV set-up and the

inner structure of the flame was determined using chemiluminescence.

2.1.1 The PIV set up

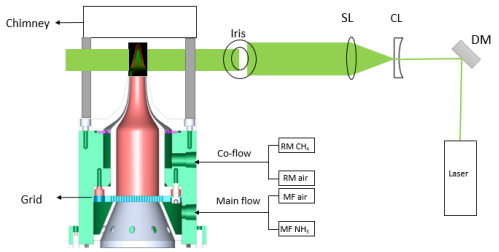

Fig. 1. Schematic diagram of the experimental set-up along with the PIV set-up. CL: cylindrical lens, SL: spherical lens, DM: dichroic mirror, RM: rotameter, MF: mass flowmeter

The airflow is fed through a seeding system, consisting of an atomizer that produces droplets of size 1 µm. Di-ethyl-hexyl-sebacate (DEHS) which evaporates at 525 K was used to seed the fresh gases with droplets. The PIV set-up consists of a laser source directed to a dichroic mirror kept at 45°. The light source used is a continuous Coherent Verdi G20 Laser of 532 nm. A laser power of 5 W is used. The light from this source is reflected at the mirror at a right angle penetrating through a cylindrical lens and then a spherical lens of a focal length, f = 750 mm providing a laser sheet perpendicular to the flame. An iris is used to control the size of the laser sheet projected on the burner to ensure that only the flame is illuminated by the laser. A CMOS high-speed camera (PHANTOM V1611) is used to capture the images and a code written in Python is used to track the particles and provide a velocity field map. A PIV interrogation window size of 32 pix^2 is set initially. Finally, an interrogation window size of 16 pix^2 with a 50% overlap is used. The conversion factor is 4.56 x 10^{-2} mm/pix and the camera acquisition rate and the exposure time were set to 10000 fps and 99 µs respectively. Fig. 1 represents the schematic diagram of the set-up.

.

2.1.2 The chemiluminescence set-up

The filters used for NH* and NH_2* are centered at wavelengths 337 nm and 632 nm respectively with a diameter of 50 mm and a bandpass width of 10 nm. The filter is placed in front of the high-speed IRO intensifier which is placed in front of the CMOS camera. The intensifier is used to have maximum sensitivity and to have a good image quality. An instantaneous shot is used for the study as it was seen that an average flame perturbation of over 200 images is small. The induced error % in thickness is 13% for an exposure time of 200 ms. The conversion factor is 5.76 x 10^{-2} mm/pix and the camera acquisition rate, and the gate of the intensifier was set to 1000 fps, and 0.098 ms respectively for NH_2* and 100 fps, and 0.98 ms respectively for NH*.

2.2 1D simulations in Chemkin-Pro

Upon comparison and validation of previous experimental results with the latest kinetic schemes available in the literature for ammonia combustion [16], the kinetic scheme of Stagni et al. [17] was used for the study here. This scheme uses 31 species and 203 reactions. 1D simulations of unstretched freely propagating flame were performed using the premixed laminar flame speed code. The CURV and GRAD were both set to 0.01 and the length of the computational domain was set to 2 cm.

3. Results and discussion

3.1 Flame thickness

Fig. 2 represents a nearly stoichiometric ammonia-air flame using the PIV set-up. This image was captured using NIKON D850 with a 180 mm objective lens and an exposure time set to 250 ms. It can be seen that this flame is much thicker than most hydrocarbon flames. The DEHS droplets are illuminated by the laser. When these droplets reach the 525 K isotherm, they evaporate. Thus, fresh gases are in the inner cone (in green) and the isotherm 525 K appears in Fig. 2 as the limit between the green and the orange zones. The

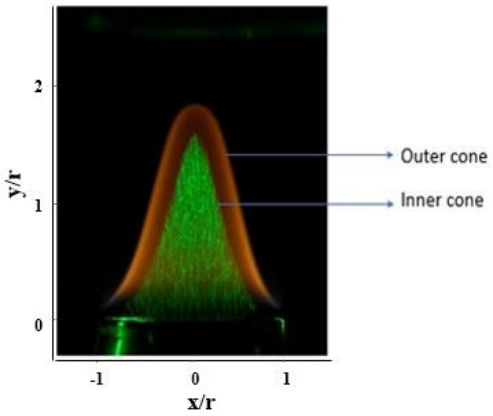

Fig. 2. Ammonia-air flame at φ= 1.1 with PIV depicting the thick flame. The inner cone and the outer cone represent the fresh gas surface and the outer flame surface respectively. The camera used to capture this image is NIKON D850 and the exposure time has been set to 250 ms. The x and y axes have been normalized over the radius of the burner axes.

outermost surface of the flame is referred to as the outer cone in Fig. 2 and is the limit between the orange and the black zones. The flame thickness,

δ, can be defined as the zone between the inner and the outer cone (between the green and the black zones in Fig. 2). The axes in Fig. 2 represent the position normalized over the burner radius with the center of the x-axis pinned at the center of the burner and the zero of the y-axis at the exit of the burner. The effect of DEHS droplets has been tested and it was seen that the evaporation of these droplets did not interfere with the parameters used in this study.

.

3.2 Flame speed determination

The most used method to evaluate flame speed for ammonia combustion available in the literature is by using a closed spherical vessel with Schlieren [18-20] and by vertical tube with direct imaging [21-22]. Han et al. [23] used the heat-flux burner method to provide the flame speed data whereas Ronney et al. [24] provided the flame speed at microgravity in a closed spherical vessel with thermocouples.

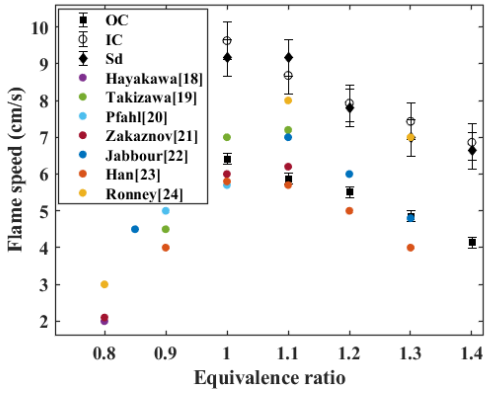

Fig. 3. Comparison of ammonia-air laminar flame speed at atmospheric conditions available in the literature for different φ. OC (black square) and IC (black circle) represent the flame speed at the outer cone and inner cone and S_d represented by black diamond is the displacement flame speed.

When the spherical flame method is used, stretch effects must be considered. The unstretched laminar flame speed is obtained by applying the continuity equation to the burning velocity and the flame ball expansion. For this calculation, the thin flame approximation is imposed i.e. it is assumed that the radii of the unburnt gases and burnt gases at the flame front are the same. Pfahl et al. and Hayakawa et al. demonstrated this in equation 4 of Ref. [20] and Ref. [18] respectively by omitting the surface area in the mass continuity equation. While considering the density of the burnt gases for this equation it is assumed that density remains homogeneous which may be true for thin flames. Tazikawa et al. used equation 1 in Ref. [19] by defining burnt mass fraction which also depends on the radius chosen. When measurements are done using a thermocouple, the distance chosen for the measurement is directly linked to the isotherm which is used to calculate the flame speed. In the case of the vertical tube method, the outermost visible layer (equivalent to the OC as shown in Fig.2) is chosen as the flame front.

The laminar flame speed, S_L, in the case of the Bunsen burner is obtained by applying conservation of mass at the exit of the burner to the inner surface and can be mathematically formulated as:

$$A_b U_{fg} \rho_{fg} = A_u S_L \rho_{fg}, \quad (1)$$

where U_{fg} is the fresh gases velocity at the burner outlet, A_b is the exit area of the burner, ρ_{fg} is the density of the fresh gases and A_u is the area of the unburnt gas surface.

The displacement speed, S_d, is defined as the propagation speed of a flame relative to the fresh gas flow and is given as:

$$S_d = (u - w).n, \quad (2)$$

where u is the fluid velocity, w is the absolute speed of the flame in a fixed laboratory and n is the flame normal vector oriented towards the fresh gases. Here, $w = 0$.

As per the definition of the flame speed, the isotherm to be chosen corresponds to the inner cone. The laminar flame speed, S_L, and the displacement speed, S_d, are computed using Equation (1) and Equation (2). The difference in the flame speed computed at the outer cone (OC) and the inner cone (IC) represented by black squares and circles respectively in Fig. 3 is around 2-3 cm s^{-1}. As shown in Fig. 3, on comparing with values given in the literature, it is seen that the flame speeds reported in the literature are closer to the flame speed obtained at the outer cone, and are far from the fresh gas isotherm. It can also be seen that the displacement speed evaluated at the inner cone which is represented by the black diamond in Fig. 3 is in congruence with the laminar flame speed at the same surface.

3.3 Curvature effects on the species

Experiments were performed for equivalence ratios between 0.9 and 1.4. Since the flow velocity is low, it can be assumed that the strain effects are negligible and the focus of the study is only on the curvature effects. Fig. 4 a and b represent the inverse Abel transformed image with the pixel intensity represented in the color bar axis for NH_2* and NH* respectively, Fig. 4 c shows the thickness of the species (NH_2* in black and NH* in violet), and Fig. 4 d displays k_1 and k_2 for NH_2*, all at φ = 1.4. k_1 represents the principal curvature along the flame (shown in blue in Fig. 4 d) and k_2 represents the principal curvature in the circumferential direction (shown in red in Fig. 4 d). By convention, negative curvature is indicated for concave front in the burned gas direction and positive curvature is for convex

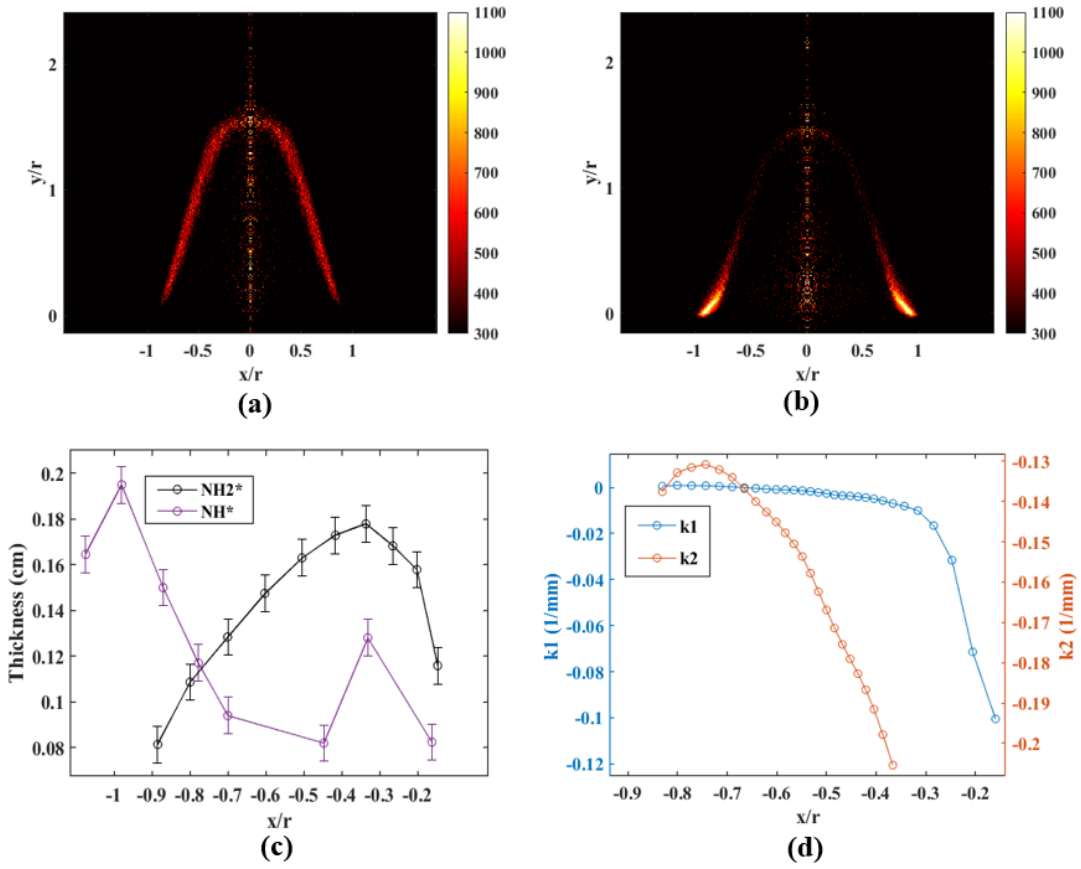

Fig. 4. NH_2* and NH* signal in an atmospheric NH_3/air flame at φ = 1.4, (a) Abel inversion transformed image of NH_2*, (b) Abel inversion transformed image of NH* with the color bar representing the pixel intensity, (c) The thickness of the species (NH_2* in black and NH* in violet) evaluated in the direction of the normal of the front vs. normalized position, (d) k_1 (blue) and k_2 (red) of NH_2* vs. normalized position.

contour in the burned gas direction. The curvature for NH_2* is only presented here to be legible to the reader. The range and the trend of both k_1 and k_2 for NH* are similar to NH_2* (NH_2* is affected slightly more than NH*). The x-axes of the plots represent the position normalized by the burner radius with the zero of the x-axes at the center of the burner. The y-axis in Fig. 4 a and b represents the position along the height normalized over the burner radius with the zero of the y-axis marking the exit of the burner. The thickness of the species was calculated as the full width at half maximum (FWHM) of the gaussian curve with a 95% confidence interval obtained when moving along the normal to front. The Abel inversion transformed images for all species at all equivalence ratio is provided in the supplementary data.

From the chemiluminescence of NH* and NH_2*, it is seen that the richer the flame, the less prominent is the curvature effect. For all conditions, except for φ = 1.1 and 1.2, it was noticed in the Abel inversion transformed images that the negative curvature at the tip of the flame does not enhance the reactivity as the average intensity remained almost constant all along the species front. Fig. 5 a, b, and c show chemiluminescence of NH* for φ= 0.9, 1.1 and 1.3 respectively whereas Fig. 5 d, e, and f show the chemiluminescence of NH_2* for φ= 1, 1.2, and 1.4. In these raw images, these effects are not visible simply because we see a 2D projection of the flame which means we see an integrated information of the species. The chemiluminescence images of all species at all equivalence ratios can be seen in the supplementary data. Since, the Lewis number increases with equivalence ratio and is close to unity [25], the effect of the negative curvature is not well pronounced at the tip of the flame, although a slightly higher effect is expected for richer flames which explains why φ= 1.1 and 1.2 witness a slight enhancement of reactivity at the flame tip. Irrespective of the excited species and the equivalence ratio of the mixture, it was observed that the species thickness continues to increase and begins to decrease when subjugated to the negative

curve (indicated by k_1) near the tip of the flame (in Fig. 4 c and d, it is seen at x/r almost equal to -0.3). The magnitude of k_2, on the other hand, increases when moving from the base of the flame to the tip of the flame. This goes to show that the mean curvature effect was simply seen as a change in thickness of the species produced if not directly the concentration of species in a given region as the average intensity remains the same (as seen in Fig. 4). The concentration of the species was spread along a larger region where k_1 was positive which was encountered near the tip of the burner for lean and near stoichiometric conditions and was concentrated over a smaller region when k_1 was negative (seen at the tip of the flame). At the tip of the flame, the contribution of k_2 is higher which gives an overall higher negative curvature effect. k_1 is relatively smaller than k_2 and is almost 0 until a distance of 0.3 times the burner radius. The stretch rate corresponding to the flame propagative/curved character, as presented in [26], K_c is proportional to the product of the mean curvature of k_1 and k_2 and the displacement speed. For ammonia-air flames, both the mean curvature and S_d are small.

On performing a species-wise comparison, it was seen that NH_2* undergoes a slightly higher mean curvature effect when compared to NH*. It was also seen that the NH_2* production was higher than that of NH* except for near the base of the flame as seen in Fig. 4 b and Fig. 5 a, b, and c and the thickness and the reactivity at this region being maximum (seen in Fig. 4 c and b respectively). It was interesting to note that the NH* production was the highest at the tip of the burner and there was no production of NH_2* in this region. Since the positive curvature at the burner exit was prominent only for lean and near stoichiometric mixture conditions, the influence of the curvature leading to higher reactivity may be ruled out as the increase in production of NH* was seen unanimously for all equivalence ratios. It was initially thought that the heat from the pilot flame promoted the direct production of NH*. Nevertheless, it was confirmed that the pilot flame did not trigger thermal decomposition to give NH as if it were the case; the production of NH_2 would also be high. A simulation performed in Chemkin-*Pro* verified that it was not thermal decomposition. This is done under the assumption that the reaction pathway to NH is through the decomposition of NH_2. There may exist a reaction pathway to produce NH directly without the formation of NH_2. It was ensured that there was no background light illumination effect. It is less likely possible that there is a presence of other species whose wavelength is within the bandpass width of the filter used as if this were to be the case, the presence of other species would be detected throughout the flame and not just at the base of the flame. The production of NH* may also be attributed to photodecomposition [27] or non-equilibrium process [28] where d'Agostino et al. employ a direct proportional relating the excited species to the non-excited species in NH_3 decomposition under R.F. plasma at moderate pressures. Another possibility could be that since NH has weaker bonds than NH_2 and since, NH is produced closer to the outer cone, it is in direct contact with the pilot flame whose temperature is about 2200 K which results in a local

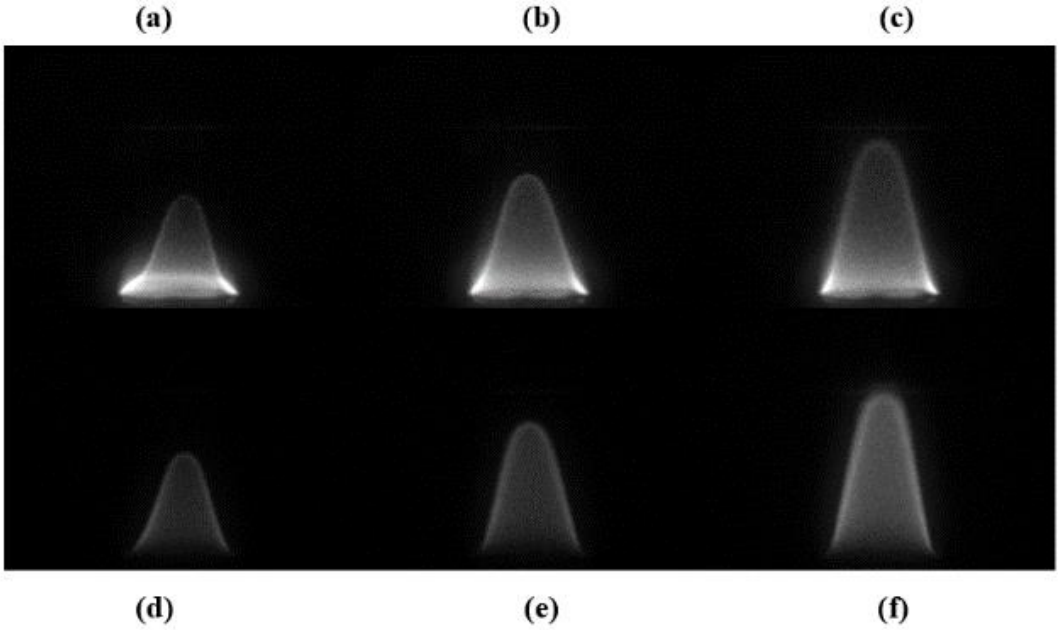

Fig. 5. Chemiluminescence images of NH* at (a) φ=0.9, (b). φ=1.1, (c) φ=1.3, and NH_2* at (d) φ=1, (e) φ=1.2, (f) φ=1.4. The exposure time of these images are not the same.

increase of collisions resulting in a brighter zone. Further investigation needs to be done to understand this observation.

3.4 Flame structure

On superimposing the excited species for each equivalence ratio with the respective PIV flame image, it is possible to trace the position of these excited species within the flame front. The evaporation of the seeding droplets gives the position of the fresh gas isotherm. Since the temperature of evaporation is already known, this isotherm corresponds to 525 K. By evaluating the position of the excited species from this isotherm along the normal of the front, the relative position of the excited species can be obtained. For φ = 0.9, 1.1, and 1.4, at a height of about 6 mm (y/r slightly less than 1) from the base of the flame where k_1 is almost zero and k_2 is near -0.2 mm^{-1} is considered as the curvature effect at this point is relatively less and maybe compared to a 1D freely propagating unstretched flame. Chemkin simulations for the kinetic scheme of Stagni were performed to make this comparison. The temperature and the heat release rate (HRR) profile along with the concentration of the non-excited species can be obtained. Fig. 6 a, b, and c represent the flame structure for φ = 0.9, 1.1, and 1.4 respectively. The fresh gas isotherm is represented as the green line. The temperature and the normalized HRR plot are shown in solid black and dashed black lines respectively. The distance along the x axis represents the a 1D domain. The species NH*, NH_2*, NH, and NH_2 are represented as cyan, magenta, blue, and, red respectively. The thickened plot for each of the species represents the standard deviation obtained when the excited species along the normal of the flame front and the non-excited species along the 1D domain is fitted into a Gaussian curve fit with a 95% confidence interval. It can be seen in the figures presented here that the species are overlapping with each other. For easy visualization, each of the species has been plotted as a quarter bar in order to minimize the overlapping between species which otherwise would have resulted in difficulty to understand the figure. The thickness of the flame front for each case

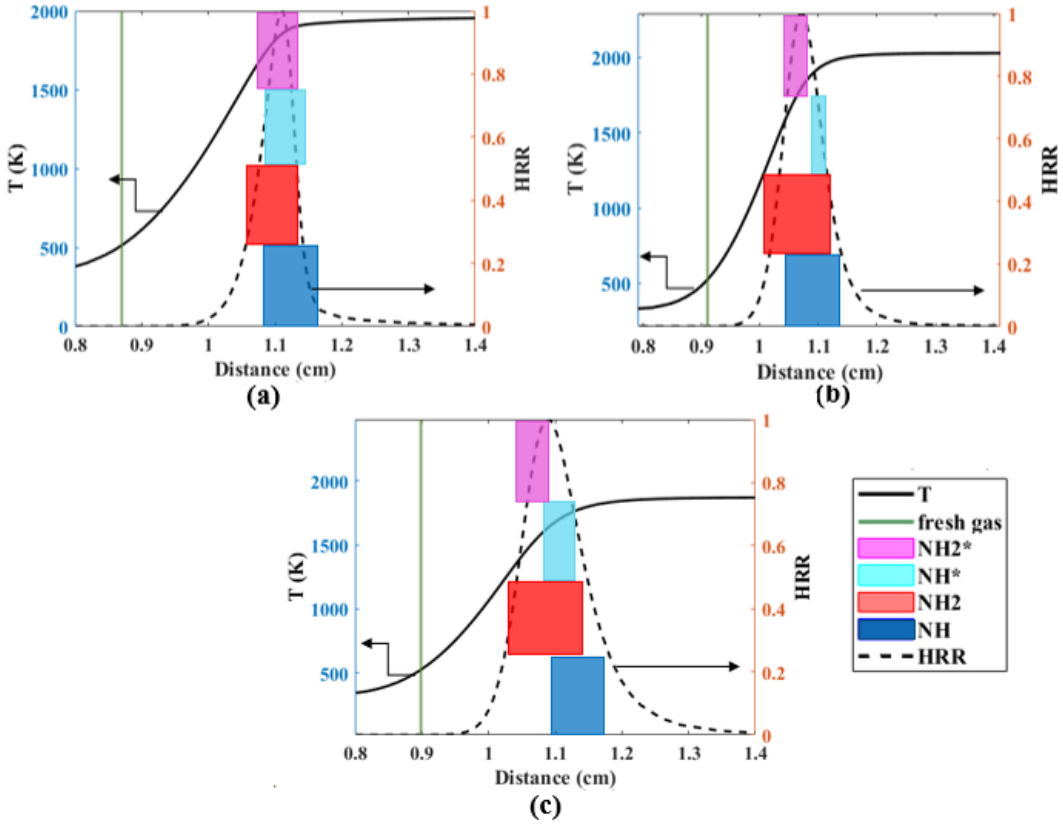

Fig. 6. Flame structure at (a) φ = 0.9, (b) φ = 1.1, (c) φ = 1.4. Temperature (solid black line) and the normalized HRR (dashed black line) are plotted on the left and the right y-axis respectively. The green line represents the fresh gas isotherm. The distance along the x-axis represents the 1D domain. Each of the species has been thickened to a width corresponding to the standard deviation of the gaussian-fit curve resulting in overlapping of the species. For easy visualization, each of the species has been plotted as a quarter bar in order to minimize the overlapping between species which otherwise would have resulted in difficulty to understand the figure.

is computed using the maximum gradient of temperature and is found to be 2.2 mm, 1.7 mm, and 2.1 mm for φ = 0.9, 1.1, and 1.4 respectively.

From Fig. 6, it can be seen that NH_2* is produced at a lower temperature than NH*. Also, both NH* and NH_2* are quite close to their corresponding non-excited species, which suggests both of the excited species are mostly formed by collisions. Thus, a collisional mechanism could be incorporated in any of the kinetic schemes. Including these species is beyond the scope of this paper due to the lack of sufficient quantitative data. The maximum HRR occurs between NH* and NH_2* for each of the cases. Therefore, the product of NH* and NH_2* is a good indicator of determining the maximum HRR experimentally. This is indeed, truly a cost-effective way of determining the HRR position.

4. Conclusion

The non-negligible thickness of atmospheric ammonia/air flames has been highlighted in this work which implies that the thin flame approximation cannot be used. The dependence of the flame speed on the isotherm and the difference in the flame speed by choosing the fresh gases surface and the outer surface of the flame has been noted. To remain consistent with the theoretical definition of the flame speed, the isotherm to be chosen has to correspond to that of the fresh gases. The laminar flame speed for ammonia-air flame on a Bunsen burner at atmospheric conditions for equivalence ratios, φ = 1-1.4 by choosing the right surface has been evaluated. Evaluating the flame speed for the case of φ = 0.9 has not been presented here owing to its large error bars.

The curvature effects on both NH* and NH_2* for φ = 0.9-1.4 have been studied. It was seen that the curvature indirectly affects the production of species by modifying the thickness of the species. When $k_1>0$, the thickness of the species is more than when compared to $k_1<0$. The curvature effects are stronger for lean flames. Since the flow is of low velocity, the strain effects can be neglected and the focus of the study has been only on the curvature effects. On comparing the species from the experiment at a height where the curvature effects are relatively lower to a 1D freely propagating flame, the structure of the ammonia-air flame at atmospheric conditions for different equivalence ratios has been studied. It may be concluded that both NH* and NH_2* are mostly produced by collision reactions of their counterpart non-excited species. The position of the maximum HRR can be determined experimentally from the position of these two excited species.

Acknowledgments

The authors are thankful to the Université d'Orléans, Region Centre-Val de Loire, and CNRS.

Supplementary material

Supplementary material has been provided.

References

[1] H. Kobayashi, A. Hayakawa, K.D.K.A. Somarathne, E.C. Okafor, Science and technology of ammonia combustion, *Proc. Combust. Inst.* 37 (2019) 109-133.

[2] X. Zhu, A.A. Khateeb, W.L. Roberts, T.F. Guiberti, Chemiluminescence signature of premixed ammonia-methane-air flames, *Combust. Flame* 231 (2021) 111508.

[3] A. Valera-Medina, M. Gutesa, H. Xiao, D. Pugh, A. Giles, B. Goktepe, R. Marsh and P. Bowen, Premixed ammonia/hydrogen swirl combustion under rich fuel conditions for gas turbines operation, *Int. J. Hydrog. Energy* 44 (2019) 8615-8626.

[4] D. Pugh, J. Runyon, P. Bowen, A. Giles, A. Valera-Medina, R. Marsh, B. Goktepe and S. Hewlett, An investigation of ammonia primary flame combustor concepts for emissions reduction with OH*, NH2* and NH* chemiluminescence at elevated conditions, *Proc. Combust. Inst.* 38 (2021) 6451-6459.

[5] X. Zhu, A. A. Khateeb, T. F. Guiberti and W. L. Roberts, NO and OH* emission characteristics of very-lean to stoichiometric ammonia–hydrogen–air swirl flames, *Proc. Combust. Inst.* 38 (2021) 5155-5162.

[6] J. Choe, W. Sun, T. Ombrello, C. Carter, Plasma assisted ammonia combustion: Simultaneous NO_x reduction and flame enhancement, *Combust. Flame* 228 (2021) 430-432.

[7] S. Wiseman, M. Rieth, A. Gruber, J. R. Dawson, J. H. Chen, A comparison of the blow-out behavior of turbulent premixed ammonia/hydrogen/nitrogen-air and methane–air flames, *Proc. Combust. Inst.* 38 (2021) 2869-2876.

[8] M.O. Vigueras-Zúñiga, M.E. Tejeda-del-Cueto, S. Mashruk, M. Kovaleva, C. L. Ordóñez-Romero, A. Valera-Medina, Methane/Ammonia radical formation during high temperature reactions in swirl burners, *Energies* 14 (2021) 6624.

[9] C. Netzer, A. Ahmed, A. Gruber, T. Løvås, Curvature effects on NO formation in wrinkled laminar ammonia/hydrogen/nitrogen-air premixed flames, *Combust. Flame* 232 (2021) 111520.

[10] S. Colson, Y. Hirano, A. Hayakawa, T. Kudo, H. Kobayashi, C. Galizzi, D. Escudié, Experimental and numerical study of NH_3/CH_4 counterflow premixed and non-premixed flames for various NH_3 mixing ratios, *Combust. Sci. Technol.* 193 (2021) 2872.

[11] R.C. Rocha, S. Zhong, L. Xu, X.S. Bai, M. Costa, X. Cai, H. Kim, C. Brackmann, Z. Li, et al., Structure and laminar flame speed of an ammonia/methane/air premixed flame under varying pressure and equivalence ratio, *Energy Fuels* 35 (2021) 7179-7192.

[12] C. Duynslaegher, H. Jeanmart, J. Vandooren, Flame structure studies of premixed ammonia /hydrogen/oxygen/argon flames: Experimental and numerical investigation, *Proc. Combust. Inst.* 32 (2009) 1277-1284.

[13] C. Brackmann, V.A. Alekseev, B. Zhou, E. Nordström, P.E. Bengtsson, Z. Li, M. Aldén, A.A. Konnov, Structure

of premixed ammonia + air flames at atmospheric pressure: Laser diagnostics and kinetic modeling, *Combust. Flame* 163 (2016) 370-381.

[14] H.G. Wolfhard and W.G. Parker, A spectroscopic investigation into the structure of diffusion flames, *Proc. Phys. Soc.* 65 (1952) 302.

[15] A. Hayakawa, T. Goto, R. Mimoto, T. Kudo, H. Kobayashi, NO formation/reduction mechanisms of ammonia/air premixed flames at various equivalence ratios and pressures, *JSME*. 2 (2015) 14-00402.

[16] A. Karan, G. Dayma, C. Chauveau, F. Halter, Experimental study and numerical validation of oxy-ammonia combustion at elevated temperatures and pressures, *Combust. Flame* 236 (2022) 111819.

[17] A. Stagni, C. Cavallotti, S. Arunthanayothin, Y. Song, O. Herbinet, F. Battin-Leclerc and T. Faravelli, An experimental, theoretical and kinetic-modeling study of the gas-phase oxidation of ammonia, *React. Chem. Eng.* 5 (2020) 696-711.

[18] A. Hayakawa, T. Goto, R. Mimoto, Y. Arakawa, T. Kudo, H. Kobayashi, Laminar burning velocity and Markstein length of ammonia/air premixed flames at various pressures, *Fuel* 159 (2015) 98-106.

[19] K. Takizawa, A. Takahashi, K. Tokuhashi, S Kondo, A. Sekiya, Burning velocity measurements of nitrogen-containing compounds, *J. Hazard. Mater.* 155 (2008) 144–152.

[20] U.J. Pfahl, M.C. Ross, J.E. Shepherd, K.O. Pasamehmetoglu, C. Unal, Flammability limits, ignition energy, and flame speeds in H2–CH4–NH3–N2O–O2–N2 mixtures, *Combust. Flame* 123 (2000) 140–158.

[21] F.Z. Zakaznov, L.A. Kursheva, ZI Felina, Determination of normal flame velocity and critical diameter of flame extinction in ammonia–air mixture. *Combust. Explos. Shock Waves* 14 (1978) 710–803.

[22] T. Jabbour , D.F. Clodic , J. Terry , S. Kondo , Burning velocity and refrigerant flammability classification, ASHRAE Trans. 110 (2004) 522–533.

[23] X. Han, Z. Wang, M. Costa, Z. Sun, Y. He, K. Cen, Experimental and kinetic modeling study of laminar burning velocities of NH_3/air, NH_3/H_2/air, NH_3/CO/air and NH_3/CH_4/air premixed flames, *Combust. Flame* 206 (2019) 214.

[24] P.D. Ronney, Effect of chemistry and transport properties on near-limit flames at microgravity, *Combust. Sci. Technol.* 59 (1988) 123–141.

[25] R. Ichimura, K. Hadi, N. Hashimoto, A. Hayakawa, H. Kobayashi, O. Fujita, Extinction limits of an ammonia/air flame propagating in a turbulent field, *Fuel* 246 (2019) 178-186.

[26] F. Thiesset, F. Halter, C. Bariki, C. Lapeyre, C. Chauveau, I. Gokalp, L. Selle, T. Poinsot, Isolating strain and curvature effects in premixed flame/vortex interactions, *J. Fluid Mech.* 831 (2017) 618-654.

[27] A.H. White and W. Melville, The decomposition of ammonia at high temperatures, *J. Am. Chem. Soc.* 27 (1905) 373-386.

[28] R. d'Agostino, F. Cramarossa, S. De Benedictis and G. Ferraro, Kinetic and spectroscopic analysis of NH_3 decomposition under R.F. plasma at moderate pressures, *Plasma Chem. Plasma Process.* 1 (1981) 19.